

THE HIGHLY IONIZED CIRCUMGALACTIC MEDIUM IS KINEMATICALLY UNIFORM AROUND GALAXIES

NIKOLE M. NIELSEN¹, GLENN G. KACPRZAK¹, SOWGAT MUZAHID^{2,3}, CHRISTOPHER W. CHURCHILL⁴, MICHAEL T. MURPHY¹, AND JANE C. CHARLTON²

¹ Centre for Astrophysics and Supercomputing, Swinburne University of Technology, Hawthorn, Victoria 3122, Australia; nikolenielsen@swin.edu.au

² Department of Astronomy & Astrophysics, The Pennsylvania State University, State College, PA 16801, USA

³ Leiden Observatory, Leiden University, PO Box 9513, NL-2300 RA Leiden, The Netherlands

⁴ Department of Astronomy, New Mexico State University, Las Cruces, NM 88003, USA

Accepted for publication in *ApJ* on November 22nd, 2016

ABSTRACT

The circumgalactic medium (CGM) traced by OVI $\lambda\lambda 1031, 1037$ doublet absorption has been found to concentrate along the projected major and minor axes of the host galaxies. This suggests that OVI traces accreting and outflowing gas, respectively, which are key components of the baryon cycle of galaxies. We investigate this further by examining the kinematics of 29 OVI absorbers associated with galaxies at $0.13 < z_{\text{gal}} < 0.66$ as a function of galaxy color, inclination, and azimuthal angle. Each galaxy was imaged with *HST* and the absorption was detected in COS/*HST* spectra of nearby ($D < 200$ kpc) background quasars. We use the pixel-velocity two-point correlation function to characterize the velocity spread of the absorbers, which is a method used previously for a sample of MgII absorber–galaxy pairs. The absorption velocity spread for OVI is more extended than MgII, which suggests that the two ions trace differing components of the CGM. Also contrary to MgII, the OVI absorption velocity spreads are similar regardless of galaxy color, inclination, and azimuthal angle. This indicates that the kinematics of the high ionization gas is not strongly influenced by the present star formation activity in the galaxy. The kinematic homogeneity of OVI absorption and its tendency to be observed mainly along the projected galaxy major and minor axes is likely due to varying ionization conditions and gas densities about the galaxy. Gas in intermediate azimuthal angles may be ionized out of the OVI phase, possibly resulting in an azimuthal angle dependence on the distribution of gas in higher ionization states.

Subject headings: galaxies: halos — quasars: absorption lines

1. INTRODUCTION

The circumgalactic medium (CGM) is a massive reservoir of multiphase gas surrounding a galaxy, with a gas mass comparable to the gas mass in the galaxy itself (Thom et al. 2011; Tumlinson et al. 2011; Werk et al. 2013; Peebles et al. 2014). It regulates the star formation rate of the galaxy through a balance of inflows and outflows into, out of, and through the CGM (e.g., Oppenheimer & Davé 2008; Lilly et al. 2013). For these reasons, understanding the multiphase nature, locations, and kinematic properties of gas in the CGM is crucial to understanding how galaxies evolve to form the galaxies observed today.

Much of the current understanding of the CGM comes from the low-ionization MgII $\lambda\lambda 2796, 2803$ doublet absorption in background quasar spectra due to it being easily observable from the ground in optical wavelengths at $z \sim 1$. Recent work has found that MgII absorbers are preferentially located along the projected major and minor axes of their host galaxies (Bordoloi et al. 2011; Bouché et al. 2012; Kacprzak et al. 2012; Lan et al. 2014) and their kinematics show distinct differences with galaxy orientation, color, and other properties (Nielsen et al. 2015, 2016). MgII is commonly associated with outflows (e.g., Rubin et al. 2010, 2014; Bouché et al. 2012; Martin et al. 2012; Bordoloi et al. 2014a,b; Kacprzak et al. 2014) and accretion or recycled outflows (e.g., Steidel et al. 2002; Kacprzak et al. 2010; Stewart et al. 2011; Martin et al. 2012; Rubin et al. 2012; Bouché et al. 2013; Ford et al. 2014).

However, given the multiphase nature of the CGM, MgII traces only a fraction of the CGM. The high-ionization OVI $\lambda\lambda 1031, 1037$ doublet absorption is another common tracer of the CGM. Tumlinson et al. (2011) has shown that

the presence of OVI is governed by the star formation rate of the host galaxy, with more absorbers associated with star forming galaxies and more nonabsorbers with passive galaxies. OVI has been further studied extensively (e.g., Wakker & Savage 2009; Prochaska et al. 2011; Johnson et al. 2013, 2015; Stocke et al. 2013; Mathes et al. 2014; Savage et al. 2014), but the physical processes giving rise to the gas traced by OVI is still debated.

Recently, Oppenheimer et al. (2016) examined circumgalactic oxygen in the EAGLE simulations. They found that OVI is not the dominant ionization state of oxygen in galaxy halos, and that the column densities of OVI peak for L_* galaxies, with lower column densities for lower and higher mass halos. Given this, the authors suggest that OVI is primarily a tracer of the virial temperature of a galaxy, where L_* galaxies have a virial temperature that results in the largest OVI ionization fraction. For galaxies less massive than an L_* galaxy, the virial temperature is too cool for strong OVI and more massive galaxies ionize the oxygen into higher ionization states. The authors also found no connection between star formation and the OVI out to 150 kpc, where the median “age” of OVI is greater than 5 Gyrs. Consequently, the Tumlinson et al. (2011) results may be reflecting the changing ionization conditions with galaxy mass rather than a star formation rate dependence.

Comparing the properties of and processes depositing both the low-ionization gas traced by MgII and the high-ionization gas traced by OVI have become more common. For example, Muzahid et al. (2015) studied an absorber–galaxy pair in detail, where the pair has both MgII and OVI absorption probed along the minor axis of an edge-on galaxy. The authors con-

cluded that the low- and high-ionization absorption traced recycled accretion and outflows, respectively. The metallicities of the ions are different, with the high-ionization phase having a metallicity (super-solar) over an order of magnitude greater than the low-ionization phase.

Using mock quasar absorption-line observations in hydrodynamic cosmological simulations, [Churchill et al. \(2015\)](#) examined the properties of the multiphase gas in the circumgalactic medium of a dwarf galaxy. The authors traced the line-of-sight spatial locations of the cells that dominate the absorption profiles. They found that while C IV and O VI are observed at similar velocities as H I and Mg II, the higher ionization gas traces different structures in different locations (spread over up to 100 kpc) along the line of sight. Also studying the simulated CGM, [Ford et al. \(2014\)](#) found that O VI primarily traces “ancient outflows” in which the gas was ejected from the galaxy by outflows greater than 1 Gyr prior to $z = 0.25$. In contrast, they found that Mg II is dominated by recycled accretion.

[Kacprzak et al. \(2015\)](#) measured the orientations (inclinations and azimuthal angles) of galaxies associated with both O VI absorbers and non-absorbers. They define an azimuthal angle of $\Phi = 0^\circ$ as having the background quasar sightline aligned with the projected galaxy major axis, and $\Phi = 90^\circ$ as the sightline along the projected galaxy minor axis. The authors reported that detected O VI absorption is preferentially found along the major and minor axes of the host galaxy (similar to the behavior of Mg II; [Kacprzak et al. 2012](#)), suggesting that the absorbers in these regions traced accretion/recycling and outflows, respectively. Absorption was rarely detected within azimuthal angles of 30° to 60° , with the authors proposing that O VI is not mixed throughout the CGM. The equivalent widths of absorption were also found to be greater along the minor axis than the major axis, hinting that the velocity spreads, the column densities, or both were dependent on the azimuthal angle at which gas is probed. To further examine the physics involved and the gas properties in relation to the galaxy, we study the kinematics of these O VI absorbers here.

Both [Nielsen et al. \(2016\)](#) and [Nielsen et al. \(2015\)](#) (hereafter MAGIIICAT IV and MAGIIICAT V, respectively) used the pixel-velocity two-point correlation function (TPCF) method for Mg II absorbers to examine the velocity spreads as a function of galaxy color, redshift, impact parameter, inclination, and azimuthal angle. The TPCF method produced clear results in which the greatest absorber velocity dispersions were located along the projected minor axis ($\Phi \geq 45^\circ$) of face-on ($i < 57^\circ$) blue galaxies. These large velocity dispersions were attributed to bipolar outflows, which, for the largest velocity dispersions, are pointed nearly directly towards or away from the observer. Red galaxies did not show these large dispersions, and in fact, showed the smallest velocity dispersions out of all subsamples, indicating a lack of outflowing material in Mg II. In this paper, we now use this TPCF method on a sample of 29 O VI absorbing galaxies as a function of galaxy color, inclination, and azimuthal angle. We also compare the O VI TPCFs to the previous results with Mg II.

This paper is organized as follows: Section 2 describes the O VI sample and data analysis to obtain the galaxy and absorption properties. We also briefly describe the pixel-velocity two-point correlation function (TPCF) method. Section 3 presents the results of examining the TPCFs of O VI absorbers as a function of galaxy color, azimuthal angle, and inclination. We also present the TPCFs for our Mg II sample (MAGIIICAT

IV and V) in this section for comparison between ions. In Section 4 we discuss our results in the context of previous work. Finally, Section 5 summarizes and concludes our findings. Throughout the paper we use AB magnitudes and a Λ CDM cosmology ($H_0 = 70 \text{ km s}^{-1} \text{ Mpc}^{-1}$, $\Omega_M = 0.3$, $\Omega_\Lambda = 0.7$).

2. SAMPLE AND DATA ANALYSIS

In this section, we describe the galaxy properties and the quasar spectra for our O VI absorber–galaxy sample, which is the focus of this paper. We also briefly describe the Mg II sample published in MAGIIICAT IV and V, which we use here for comparison to the more highly ionized O VI CGM. Finally, we briefly describe our pixel-velocity TPCF method for studying the absorption kinematics.

2.1. Galaxy Properties

We use the subset of 29 galaxies with colors and detected O VI $\lambda\lambda 1031, 1037$ doublet absorption from the sample presented in [Kacprzak et al. \(2015\)](#) (hereafter Kacprzak15), which were identified as part of our “Multiphase Galaxy Halos” large *HST* program (e.g., [Kacprzak15](#), [Muzahid et al. 2015, 2016](#)) or obtained from the literature. The galaxies with non-detections in O VI reported in Kacprzak15 are not included here as we cannot measure their absorption kinematics. The absorption-selected galaxies are located at spectroscopic redshifts of $0.13 < z_{\text{gal}} < 0.66$ (median $\langle z_{\text{gal}} \rangle = 0.244$) and within an on-the-sky projected distance of $D \sim 200 \text{ kpc}$ ($21.1 \text{ kpc} < D < 203.2 \text{ kpc}$, $\langle D \rangle = 93.2 \text{ kpc}$) from a background quasar. These are isolated galaxies, where no neighbors were identified within a projected distance of 200 kpc from the quasar line-of-sight and within a line-of-sight velocity separation of 500 km s^{-1} .

We have modified the Kacprzak15 sample slightly in a few cases. The sample we use is summarized in Table 1, and the changes are as follows. The J121920 absorber–galaxy pair is excluded here due to a highly uncertain azimuthal angle measurement. We calculated galaxy colors for two additional galaxies using magnitudes obtained from NED¹: J100402 ($u - r = 1.00$) and J111908 ($B - K = 2.21$). Lastly, the colors quoted by Kacprzak15 for the J045608 galaxies are transposed in their Table 2; the values are published correctly in [Nielsen et al. \(2013b\)](#).

After followup observations with ESI/Keck spectra, we found that the impact parameters of the two J1233–0031 galaxies ($z_{\text{gal}} = 0.4174$ and $z_{\text{gal}} = 0.3185$) reported by [Werk et al. \(2012\)](#) appear to be transposed. The $z_{\text{gal}} = 0.3185$ galaxy, which is included here, is located at $D = 85 \text{ kpc}$ rather than $D = 31 \text{ kpc}$. This error is propagated in Kacprzak15, and the reported inclination and azimuthal angle measurements should be $i = 38.7^\circ$ and $\Phi = 17.0^\circ$, respectively. This, however, does not significantly change their results. We also later found that one of the galaxies listed in the Kacprzak15 sample is located in a group environment: Q0122–003, $z_{\text{gal}} = 0.3787$, with a neighboring galaxy at $z_{\text{gal}} = 0.3792$. It is also listed in the MAGIIICAT sample as an isolated galaxy, though we do not have a HIRES or UVES quasar spectrum for the associated absorber so it is not included in the MAGIIICAT IV or V analyses. For the work presented here, we do not use this galaxy and have moved it to a group sample for later analysis.

Each of the 29 galaxies in our sample was imaged with WFPC2, WFC3, or ACS on the *Hubble Space Telescope*

¹ <https://ned.ipac.caltech.edu/>

Table 1
Galaxy Properties

Field	z_{gal}	D (kpc)	$B-K$	i (deg)	Φ (deg)
J012528-000555	0.3985	163.0	1.80	63.2	59.3
J035128-142908	0.3567	72.2	0.28	28.5	4.8
J045608-215909	0.3818	103.4	1.78	57.1	63.7
J045608-215909	0.4847	108.0	1.66	42.1	85.2
J091440+282330	0.2443	105.8	1.48	38.9	18.2
J094331+053131	0.3530	96.4	1.40	44.3	8.1
J094331+053131	0.5480	150.8	1.17	58.8	67.1
J095000+483129	0.2119	93.5	3.13	47.7	16.6
J100402+285535	0.1380	56.7	1.21	79.1	12.3
J100902+071343	0.2278	63.9	1.39	66.2	89.5
J104116+061016	0.4432	56.2	2.81	49.8	4.2
J111908+211918	0.1380	137.9	2.21	26.3	34.4
J113327+032719	0.1545	55.6	1.53	23.5	56.0
J113910-135043	0.2044	93.1	2.30	83.4	5.8
J113910-135043	0.2123	174.8	2.10	84.9	80.4
J113910-135043	0.2198	121.9	2.42	85.0	44.9
J113910-135043	0.3191	73.2	1.60	83.3	39.0
J123304-003134	0.3185	88.9	1.63	38.6	17.0
J124154+572107	0.2053	21.1	1.67	56.4	77.6
J124154+572107	0.2178	94.5	1.80	17.4	62.9
J124410+172104	0.5504	21.2	1.34	31.6	20.1
J130112+590206	0.1967	135.4	1.87	80.7	39.7
J131956+272808	0.6610	103.8	1.45	65.8	86.6
J132222+464546	0.2142	38.5	2.33	57.8	13.8
J134251-005345	0.2270	35.2	1.86	0.1	13.1
J135704+191907	0.4592	45.4	1.40	24.7	64.2
J155504+362847	0.1893	33.4	1.69	51.8	47.0
J213135-120704	0.4300	48.4	2.06	48.3	14.9
J225357+160853	0.3529	203.1	1.30	36.7	88.7

(*HST*) and their morphological properties were modeled using GIM2D (Simard et al. 2002). Full details of the galaxies and their modeling are described in Kacprzak15. We define an inclination of $i = 0^\circ$ as face-on and $i = 90^\circ$ as edge-on. An azimuthal angle of $\Phi = 0^\circ$ indicates that the background quasar sightline is aligned with the projected galaxy major axis, and $\Phi = 90^\circ$ indicates the sightline is aligned with the projected galaxy minor axis.

Galaxy $u-r$ colors from Kacprzak15, plus an additional $u-r$ color obtained from NED, were converted to $B-K$ colors following similar methods described in Nielsen et al. (2013b, MAGIIICAT I) for direct comparison to the Mg II sample studied in MAGIIICAT IV and V, which uses $B-K$ colors. Colors for each galaxy spectral energy distribution (SED) were calculated and we obtained a linear least-squares fit of $(B-K) = 1.10(u-r) + 0.113$ to the galaxy SED colors. We then applied this relation to the $u-r$ colors to have a uniform set of $B-K$ colors, and the new values are listed in Table 1.

In order to examine the absorber kinematics for galaxies as a function of different baryon cycle processes and star formation rates, we form various subsamples by using the median galaxy property values of the sample. For the orientation measurements, these values are $\langle i \rangle = 51^\circ$ and $\langle \Phi \rangle = 45^\circ$. Using the average inclination of galaxies in the universe, as was done in MAGIIICAT V, is not feasible here because the subsample

sizes with that cut would not be balanced. The uncertainties on the orientation measurements are small enough such that only one galaxy could potentially shift from being assigned to the minor axis subsample to being assigned to the major axis subsample, and only two galaxies could shift from face-on to edge-on.

The median galaxy color of the sample is $\langle B-K \rangle = 1.66$. This value is used to compare between galaxies that are more likely to be star-forming or passive rather than with galaxy morphological types or with the color bimodality of galaxies in the universe. Comparing the absorption associated with blue galaxies to that associated with red galaxies is important because previous work has shown that the equivalent widths (which depend on the velocity width and column density of the gas) of low-ionization Mg II absorbers depend on some measure of the star formation rate (e.g., Zibetti et al. 2007; Bordoloi et al. 2011; Rubin et al. 2014). Tumlinson et al. (2011) found that OVI, which is the focus here, also depends on the SFR of the host galaxy, where star-forming galaxies nearly always have detected absorption and passive galaxies rarely have detected absorption. Since we do not currently have star formation rates, we rely on galaxy color as a proxy for comparison to the Tumlinson sample.

The cut used here, $\langle B-K \rangle = 1.66$, is roughly consistent with the boundary between star-forming OVI absorbing galaxies and passive OVI non-absorbing galaxies. Kacprzak15 show that the boundary between mostly OVI absorbing and mostly OVI non-absorbing galaxies is roughly at $B-K = 1.6$ (same for $u-r$). While Kacprzak15 do not have the star formation rates of the galaxies, this cut is consistent with Tumlinson et al. (2011).

The subsample cuts, median redshift, and number of galaxies in each subsample are listed in Table 2. We also list the subsample cuts for the Mg II subsamples from MAGIIICAT IV and V for comparison.

There are no significant correlations between galaxy properties in the sample. There are also no biases with azimuthal angle or inclination; a one-dimensional Kolmogorov-Smirnov (KS) test reports that the azimuthal angles and inclinations of the galaxies are consistent with unbiased samples at the 0.6σ and 2.6σ levels, respectively.

2.2. Quasar Spectra

The galaxies described in the previous section are associated with absorption in 23 quasars. Each quasar has a medium resolution ($R \sim 20,000$, FWHM $\sim 18\text{km s}^{-1}$) spectrum from COS/*HST*, which covers the detected OVI $\lambda\lambda 1031, 1037$ doublet at the redshifts of the targeted galaxies. Full details of the spectra, their reduction, and the modeling of absorption are listed in Kacprzak15. Each OVI $\lambda\lambda 1031, 1037$ doublet was Voigt profile (VP) fitted, simultaneously when possible to account for blends, using VPFIT.² Velocity zero points (i.e., z_{abs}) were defined as the median velocity of the optical depth distribution of absorption for the OVI $\lambda 1031$ line. The OVI absorption doublets for the absorber-galaxy pairs are plotted in Figure 1.

The velocity range of each absorber was determined by finding the velocity or wavelength at which the VP model spectrum (rather than the actual spectrum) decreases by 1% from the continuum level. Using the VP model to define the velocity ranges is necessary since several OVI absorbers are blended with other ions and the spectra are more noisy than

² <http://www.ast.cam.ac.uk/~rfc/vpfit.html>

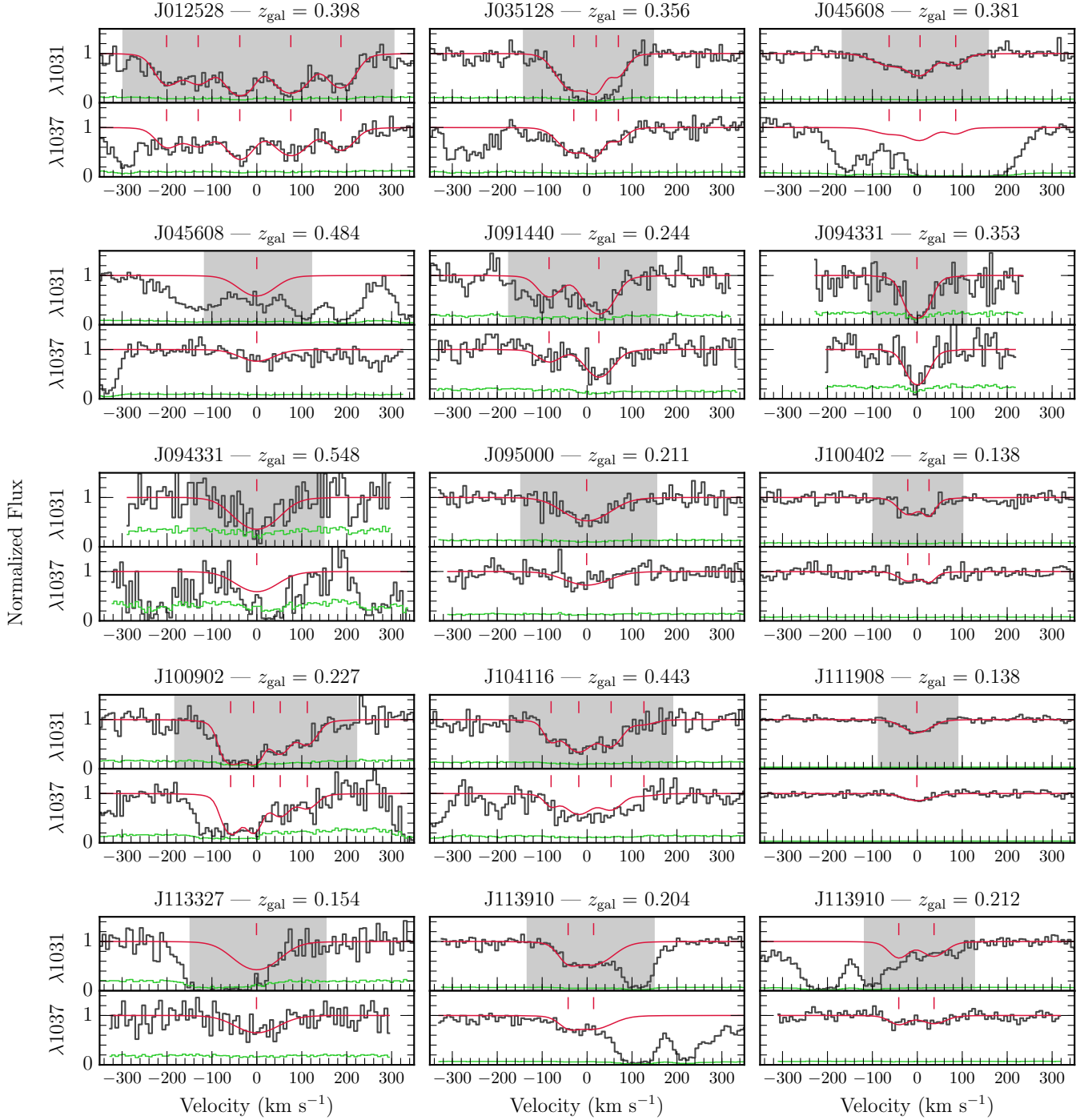


Figure 1. O VI $\lambda\lambda 1031, 1037$ doublet absorption profiles and fits for each absorber-galaxy pair in the sample. In each panel pair, the $\lambda 1031$ line is plotted on top, and the $\lambda 1037$ line on bottom. The quasar spectrum is plotted as the black histogram, the uncertainty on the spectrum is the green line, and the fit to the data is plotted as the red line. Vertical red ticks at the top of each panel show the central velocity of each Voigt profile component fitted to the data. Gray shaded regions in the top panels indicate the velocity range of the absorbers, defined in Section 2.2. For the TPCF calculations, we use only those pixels located within these shaded regions. Velocity zero points are defined as the optical depth-weighted median of absorption.

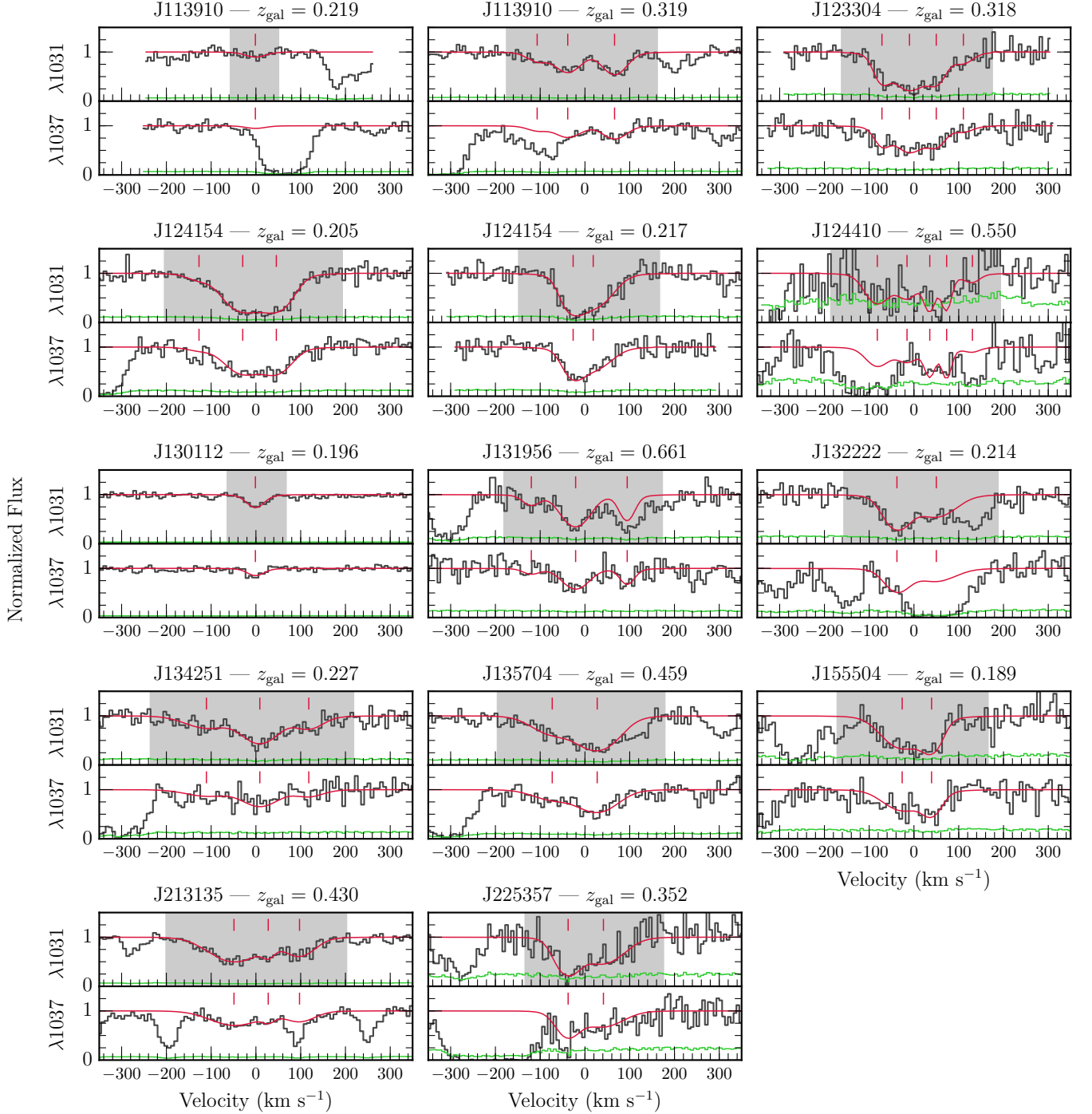


Figure 1. (Continued)

the HIRES or UVES spectra for MgII. For our analysis, we use only those pixels within these velocity bounds, which are plotted as gray shaded regions in the $\lambda 1031$ panels of Figure 1.

This method is simpler than the method used for MgII because the OVI absorbers have a less complex absorption profile; the OVI absorbers generally consist of a single broad “kinematic subsystem” while MgII may be composed of multiple kinematic subsystems (e.g., Churchill & Vogt 2001, MAGIIICAT IV, V). Only one OVI absorber (J121920) has two kinematic subsystems, but we exclude this absorber from our analysis because the associated galaxy has a highly uncer-

tain azimuthal angle measurement. When we use this velocity range determination method on the MgII absorbers from MAGIIICAT IV and V, we find comparable, or more conservative ranges (i.e., velocities closer to $v = 0 \text{ km s}^{-1}$) compared to our previous method in nearly all cases. Thus, the different methods do not produce drastically different results, and our simpler method may actually slightly underestimate the velocity extents of the OVI kinematics compared to MgII.

2.3. The MgII Comparison Sample

We compare the OVI absorber kinematics to the MgII absorber kinematics published in MAGIIICAT IV and V. Here we briefly describe the MgII sample and refer the reader to the MAGIIICAT series papers for further details (Nielsen et al. 2013a,b, 2015, 2016; Churchill et al. 2013).

We use a subset of 30 absorber–galaxy pairs with MgII absorption from the MgII Absorber–Galaxy Catalog (MAGIIICAT). All of these galaxies have spectroscopic redshifts ($0.3 < z_{\text{gal}} < 1.0$, $\langle z_{\text{gal}} \rangle = 0.656$), $B-K$ colors ($\langle B-K \rangle = 1.4$), and MgII absorption detected in high-resolution background quasar spectra (HIRES/Keck or UVES/VLT) within a projected distance of $D = 200$ kpc ($\langle D \rangle = 40$ kpc). Additionally, all galaxies have *HST* images with which the orientations have been measured using GIM2D (Kacprzak et al. 2011b, 2012). Of the 30 MgII absorber–galaxy pairs, only seven have associated OVI absorption and overlap with the OVI sample presented in Section 2.1. Note that the absorber–galaxy pairs in this MAGIIICAT sample have higher redshifts, bluer colors, and smaller impact parameters on average than our main OVI sample.

Subsamples for the MgII sample are determined by the median galaxy color of $\langle B-K \rangle = 1.4$, as well as orientation measurements of $i = 57^\circ$ (the mean inclination of galaxies in the universe), and $\Phi = 45^\circ$. These values and the subsample sizes are tabulated in Table 2 and are further described in MAGIIICAT IV and V.

The absorption kinematics for the MgII sample have already been fully analyzed in MAGIIICAT IV and V. We present these kinematics here for comparison, but do not present any new results.

2.4. Pixel-velocity TPCFs

To examine the absorber kinematics as a function of galaxy properties, we use the pixel-velocity TPCF method described in detail in MAGIIICAT IV and V. A summary of the method follows.

The pixel-velocity TPCF is calculated by first obtaining the velocities of all pixels within the velocity bounds of detected absorption for a subsample. A velocity of $v = 0$ km s⁻¹ corresponds to the optical depth-weighted median of absorption and defines the absorption redshift, z_{abs} . The pixel velocities for all absorbers in a subsample are pooled together as if they came from a single absorber hosted by a galaxy of a certain type, e.g., blue galaxies probed along the projected minor axis. Velocity separations between each pixel pair, without duplications, are then calculated for this pool. The absolute value of these velocity separations are then binned into 20 km s⁻¹ wide bins, which is comparable to the FWHM of COS/*HST*. The count in each bin is normalized by the total number of pixel velocity pairs in the subsample to account for varying subsamples sizes when comparing between subsamples. The pixel-velocity TPCF is thus a probability distribution function and provides a statistical view of the absorber velocity dispersion for a given galaxy subsample.

Uncertainties in the TPCFs are calculated using a bootstrap analysis with 100 realizations. The uncertainties reported are 1σ deviations from the mean of the bootstrap realizations, which allow for asymmetrical uncertainties around the true TPCFs.

To compare TPCFs between subsamples, we perform a chi-squared test, taking into account the uncertainties in the TPCFs. We also report $\Delta v(50)$ and $\Delta v(90)$ values, i.e., the velocity separation within which 50% and 90% of the area

under the TPCF curve is contained, for each TPCF to help describe where two TPCFs differ in more detail than the chi-squared test provides. These values are tabulated in Table 2. The uncertainties on $\Delta v(50)$ and $\Delta v(90)$ are calculated from the bootstrap realizations, similar to the TPCF uncertainties.

The bin sizes for the TPCFs presented here are twice as large as the TPCFs presented with MgII (MAGIIICAT IV and V) due to a coarser spectral resolution in the COS spectra compared to HIRES spectra. To test the effect that changing the TPCF bin sizes had, we reran the MgII TPCFs from MAGIIICAT IV and V with the 20 km s⁻¹ bin widths. With larger bin sizes, the general MgII TPCF results remained unchanged. These coarser MgII TPCFs are presented with the OVI TPCFs for comparison between ions.

3. RESULTS

3.1. Full Sample

3.1.1. Sample Distribution

The distribution of both OVI and MgII absorbers as a function of their orientation relative to the host galaxy is plotted in Figure 2. Panel (a) presents the azimuthal angle versus impact parameter of each absorber–galaxy pair. The galaxy for each pair is located at $D = 0$ kpc, with the major axis aligned with $\Phi = 0^\circ$. Points represent the location of the background quasar sightline. Point sizes indicate the velocity width of absorption, i.e., the difference between the extremes of the gray shaded regions in Figure 1. Point sizes can be compared between ions as both are normalized to the maximum velocity spread of the OVI absorbers.

There is an overlap of seven absorber–galaxy pairs between the MgII and OVI samples. These are presented as orange points on top of purple. We note that although the overlapping points (the differing ions) are plotted in the same locations, their z_{abs} values can differ by up to roughly 110 km s⁻¹ (for the MgII profiles, see Kacprzak et al. 2011b). The smallest velocity separation between the z_{abs} for the two ions is 27 km s⁻¹. Given that z_{abs} is the optical depth weighted median of absorption, this indicates that the absorption is distributed differently along the line of sight between the two ions.

The azimuthal angle behavior of the samples discussed in detail by Kacprzak et al. (2012) (MgII) and Kacprzak15 (OVI) appears to be present in this plot, though the trend is less obvious here. This is likely because we only present a subset of the MgII sample studied by Kacprzak et al. (2012). There is a population of absorbers for both ions within $\Phi \sim 15^\circ$ of the major axis, a slight gap, and then another, larger population at $\Phi > 35^\circ$. Interestingly, the group of three OVI absorbers located at $D \sim 140$ kpc and $30^\circ < \Phi < 45^\circ$ appear to have smaller point sizes than the rest of the OVI absorbers. As shown in Kacprzak15, the frequency of “non-detections” in OVI ($W_r(1031) < 0.1 \text{ \AA}$) is largest between $30^\circ < \Phi < 60^\circ$. In fact, these three points have $W_r(1031) < 0.1 \text{ \AA}$, the only absorbers with equivalent widths this low in the sample presented here. We refrain from investigating the azimuthal angle distribution preferences of the absorbers further as these were examined previously.

Figure 2(b) presents the impact parameter, D , as a function of inclination, i , for the MgII and OVI samples. Point sizes again represent the velocity width of absorption. The vertical dashed lines represent the inclinations by which we slice the sample into “face-on” ($i \sim 0^\circ$) and “edge-on” ($i \sim 90^\circ$) subsamples. For the MgII sample, we used the mean inclination

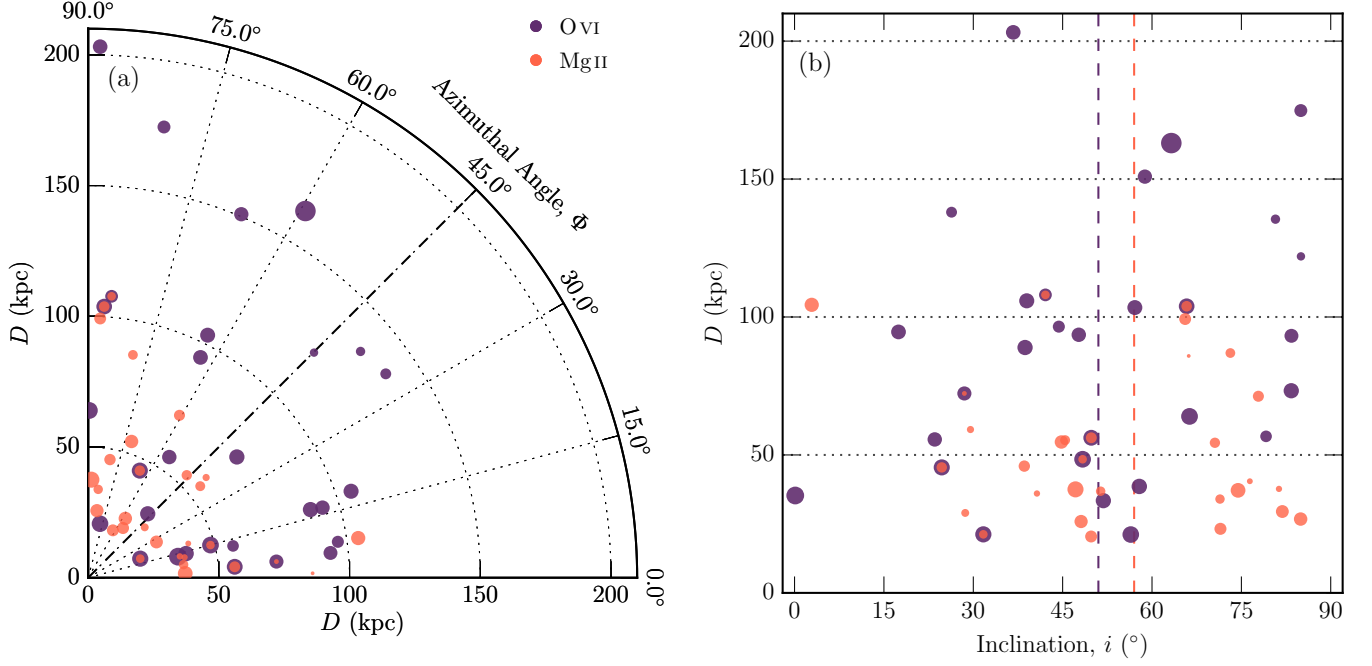


Figure 2. Galaxy orientation measures as a function of impact parameter for both OVI and MgII samples. Point sizes represent the velocity spread of the absorbers, with larger points indicating larger velocity spreads. The seven overlapping OVI and MgII points indicate absorber–galaxy pairs for which we have detected both ions. (a) Azimuthal angle versus impact parameter for both the OVI and MgII samples. Points represent the location of the quasar sightline, where the foreground galaxy in each case is located at $D = 0$ kpc and is aligned such that the major axis has $\Phi = 0^\circ$ and the minor axis has $\Phi = 90^\circ$. The dashed line at $\Phi = 45^\circ$ indicates the value by which we slice the samples into major and minor axis subsamples. (b) Inclination versus impact parameter for both ion samples. Vertical dashed lines indicate the inclinations by which the samples are sliced, with $i = 51^\circ$ for OVI and $i = 57^\circ$ for MgII. OVI absorbers tend to be located further from the galaxy, especially along the minor axis and for edge-on galaxies.

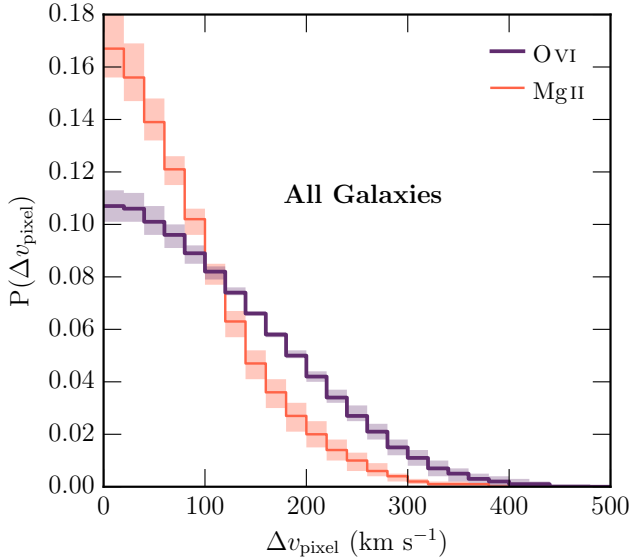


Figure 3. Pixel-velocity TPCFs for the full samples of 29 OVI and 30 MgII absorbers with the same binning for comparison between ions. The MgII absorbers come from MAGNIFICAT IV and include only those absorber–galaxy pairs with galaxy colors and orientation measurements. The thick purple line and shading indicate OVI TPCFs and uncertainties, respectively, while thin orange line and shading represent MgII. OVI absorbers have significantly larger velocity dispersions than MgII absorbers.

of galaxies in the universe, whereas here we use the median inclination of the OVI absorbers to even out subsample sizes. The MgII absorbers appear to have a larger variation in their point sizes (velocity spreads) than OVI, though this is subtle.

Also difficult to discern is the dependence of the point sizes on Φ , i , and D . We use the pixel-velocity TPCFs to examine these differences in more detail below.

3.1.2. Pixel-velocity TPCFs

As a first comparison of the kinematics between the different ions, the TPCF for the full sample of OVI absorbers is plotted as a thick purple line with shading representing errors in Figure 3. The full sample of MgII absorbers with the same binning is plotted as the thin orange line with shading representing errors. The velocity dispersion of OVI tends to be large, with pixel velocity separations up to ~ 400 km s $^{-1}$. This is in contrast to the more narrow MgII TPCF. Compared to MgII, $\Delta v(50)$ and $\Delta v(90)$ for OVI are roughly 50% and 40% larger, respectively.

It is important to keep in mind that our OVI sample of galaxies is located at lower redshifts ($\langle z_{\text{gal}} \rangle = 0.244$), is probed at greater distances on average ($\langle D \rangle = 93.2$ kpc, as shown in Figure 2), and has redder colors ($\langle B-K \rangle = 1.66$) than the MgII galaxies. We discuss these differences in Section 4. For easy comparison between the two ions, the subsample cuts and sizes for each ion are listed in Table 2 for the rest of the presented results.

3.2. Color and Orientation

The TPCFs of blue galaxies (panel (a)) and red galaxies (panel (b)) probed along the projected major and minor axes are plotted in Figure 4. There are no differences in the OVI TPCFs for either panel (0.1σ and 0.4σ) and $\Delta v(50)$ and $\Delta v(90)$ for each subsample pair are all consistent within uncertainties. For the subsample pairs not shown, the chi-squared results are 0.1σ (major axis, blue vs. red galax-

Table 2
TPCF $\Delta v(50)$ and $\Delta v(90)$ Measurements

Sample	O VI					Mg II ^a			
	Cut	Cut	$\langle z_{\text{gal}} \rangle$	# Gals	$\Delta v(50)^b$	$\Delta v(90)^b$	Cut	Cut	# Gals
Figure 3									
All Mg II Absorbers ^d	0.656 ^c	30 ^c	66 ⁺⁵ ₋₆ ^c	172 ⁺¹³ ₋₁₇ ^c
All O VI Absorbers	0.244	29	100 ⁺⁵ ₋₆	235 ⁺¹⁴ ₋₁₆
Figure 4									
Blue–Major Axis	$B-K < 1.66$	$\Phi < 45^\circ$	0.319	7	90 ⁺⁵ ₋₈	210 ⁺¹¹ ₋₂₀	$B-K < 1.4$	$\Phi < 45^\circ$	5
Blue–Minor Axis	$B-K < 1.66$	$\Phi \geq 45^\circ$	0.459	7	96 ⁺⁵ ₋₆	225 ⁺¹⁰ ₋₁₄	$B-K < 1.4$	$\Phi \geq 45^\circ$	10
Red–Major Axis	$B-K \geq 1.66$	$\Phi < 45^\circ$	0.214	9	99 ⁺⁹ ₋₈	231 ⁺²¹ ₋₁₈	$B-K \geq 1.4$	$\Phi < 45^\circ$	10
Red–Minor Axis	$B-K \geq 1.66$	$\Phi \geq 45^\circ$	0.215	6	119 ⁺¹⁷ ₋₂₁	280 ⁺³⁷ ₋₅₁	$B-K \geq 1.4$	$\Phi \geq 45^\circ$	5
Figure 5									
Blue–Face-on	$B-K < 1.66$	$i < 51^\circ$	0.353	9	91 ⁺⁴ ₋₅	212 ⁺⁹ ₋₁₃	$B-K < 1.4$	$i < 57^\circ$	8
Blue–Edge-on	$B-K < 1.66$	$i \geq 51^\circ$	0.319	5	98 ⁺⁷ ₋₈	227 ⁺¹⁶ ₋₁₇	$B-K < 1.4$	$i \geq 57^\circ$	7
Red–Face-on	$B-K \geq 1.66$	$i < 51^\circ$	0.222	6	106 ⁺⁷ ₋₁₁	246 ⁺¹⁶ ₋₂₄	$B-K \geq 1.4$	$i < 57^\circ$	9
Red–Edge-on	$B-K \geq 1.66$	$i \geq 51^\circ$	0.212	9	109 ⁺¹⁷ ₋₁₆	262 ⁺³⁸ ₋₄₀	$B-K \geq 1.4$	$i \geq 57^\circ$	6
Figure 6									
Face-on–Major Axis	$i < 51^\circ$	$\Phi < 45^\circ$	0.336	10	100 ⁺⁶ ₋₉	234 ⁺¹⁴ ₋₂₀	$i < 57^\circ$	$\Phi < 45^\circ$	10
Face-on–Minor Axis	$i < 51^\circ$	$\Phi \geq 45^\circ$	0.353	5	90 ⁺⁵ ₋₄	210 ⁺¹¹ ₋₁₀	$i < 57^\circ$	$\Phi \geq 45^\circ$	7
Edge-on–Major Axis	$i \geq 51^\circ$	$\Phi < 45^\circ$	0.209	6	80 ⁺¹⁰ ₋₁₅	187 ⁺²⁰ ₋₃₂	$i \geq 57^\circ$	$\Phi < 45^\circ$	5
Edge-on–Minor Axis	$i \geq 51^\circ$	$\Phi \geq 45^\circ$	0.305	8	116 ⁺¹² ₋₁₅	272 ⁺²⁸ ₋₃₇	$i \geq 57^\circ$	$\Phi \geq 45^\circ$	8

^a The Mg II data, analysis, results, and conclusions are published in [Nielsen et al. \(2015\)](#) and [Nielsen et al. \(2016\)](#), and references therein

^b km s⁻¹

^c Values listed are for Mg II absorbers

ies) and 0.4σ (minor axis, blue vs. red galaxies). The slightly (but not significantly) larger velocity separation tail for red galaxies in Figure 4(b) is due to a single absorber with $W_r(1031) = 0.817 \text{ \AA}$, which is an outlier in equivalent width for the sample. This unusually strong O VI equivalent width absorber was studied in detail by [Muzahid et al. \(2015\)](#), who associated the absorption with a large-scale outflow. Removing this absorber does not change the conclusions drawn from the TPCFs. The TPCFs of the Mg II absorbers for the same subsamples (MAGII-CAT V, inset panels) are comparatively more narrow, with the exception of the blue, minor axis subsample in panel (a), which has a velocity dispersion similar to the O VI.

For the TPCFs in Figure 5, which compare face-on and edge-on inclinations for blue galaxies (panel (a)) and red galaxies (panel (b)), there are again no differences in the velocity dispersions for each subsample pair ($\sim 0\sigma$ for all pairs). The $\Delta v(50)$ and $\Delta v(90)$ are also all consistent within uncertainties, and the conclusions do not change when the large equivalent width absorber is removed from the sample. In comparison, while the Mg II TPCFs (published in MAGII-CAT V, inset panels) for edge-on subsamples are consistent within uncertainties, similar to the behavior of O VI, they have smaller velocity dispersions than O VI. While the Mg II TPCF for the red, face-on galaxy subsample is also much more narrow than O VI, the Mg II TPCF for the blue,

face-on galaxy subsample is comparable to O VI.

These results indicate that the kinematics of O VI absorbers do not depend strongly on galaxy color or star formation activity for various inclinations and azimuthal angles, in contrast to Mg II absorbers as we found in MAGII-CAT V.

3.3. Inclination and Azimuthal Angle

For face-on galaxies in Figure 6(a), we find no differences (0.7σ) in the O VI TPCFs for galaxies probed along the projected major or minor axes. The $\Delta v(50)$ and $\Delta v(90)$ are consistent within uncertainties. This is in contrast to the Mg II results from MAGII-CAT V (inset panels), where face-on, major axis galaxies host absorbers with much smaller velocity dispersions. The face-on, minor axis Mg II TPCF is comparable to the O VI TPCF.

Conversely, we find significant differences in the O VI TPCFs for edge-on galaxies probed along the major and minor axes in Figure 6(b). Galaxies probed along the minor axis have larger velocity dispersions than those probed along the major axis, and this result is significant at the 4.6σ level. Both $\Delta v(50)$ and $\Delta v(90)$ for these samples are inconsistent within uncertainties. A moderate portion of this difference is caused by the $W_r(1031) = 0.817 \text{ \AA}$ absorber (an edge-on, minor axis galaxy; [Muzahid et al. 2015](#)); however, removing the absorber from the sample still results in a significance of 3.4σ , though the scatter on the edge-on, minor axis subsam-

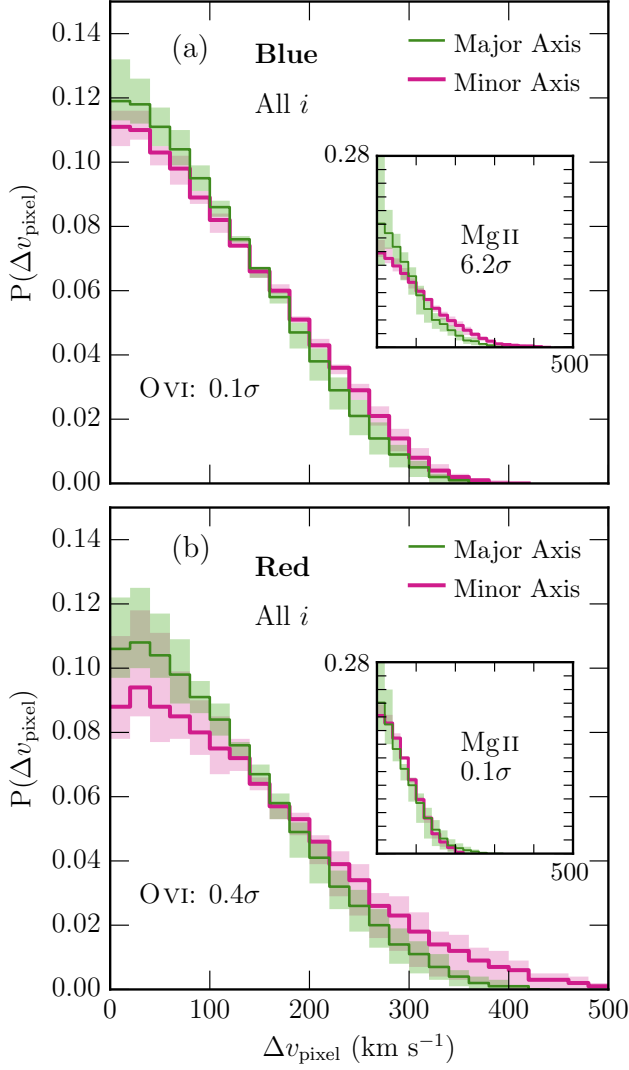


Figure 4. Pixel-velocity TPCFs for (a) blue galaxies and (b) red galaxies probed along the projected major and minor axis. The TPCFs in the main panels represent OVI, while those in the insets are for MgII. The MgII TPCFs are published in MAGIIICAT V, and are rebinned here for comparison. The inset axes range in velocity separation from 0 km s^{-1} to 500 km s^{-1} (the same as the main panel), while the probabilities range from 0 to 0.28. The OVI TPCFs show no dependence on $B-K$ nor Φ , with the highest chi-squared significance result of 0.9σ for every combination of TPCFs. The MgII TPCFs have smaller velocity dispersions for every subsample except for the blue, minor axis subsample which has velocity dispersions more similar to the higher ionization gas.

ple is significantly reduced. This result is in contrast to our previously published results with MgII (MAGIIICAT V, inset panels), which have TPCFs consistent within uncertainties. The edge-on, major axis subsample for OVI is comparable to the MgII subsamples.

For face-on and edge-on galaxies probed along the major axis (not plotted), we find an insignificant difference of 2.5σ where face-on galaxies tend to have a slightly larger velocity spread than edge-on galaxies. This behavior is opposite what we found in MgII (MAGIIICAT V), though the edge-on MgII subsample has a velocity dispersion comparable to the same OVI subsample.

Finally, for galaxies probed along the minor axis (not plotted), we find a significant difference (4.0σ) between the

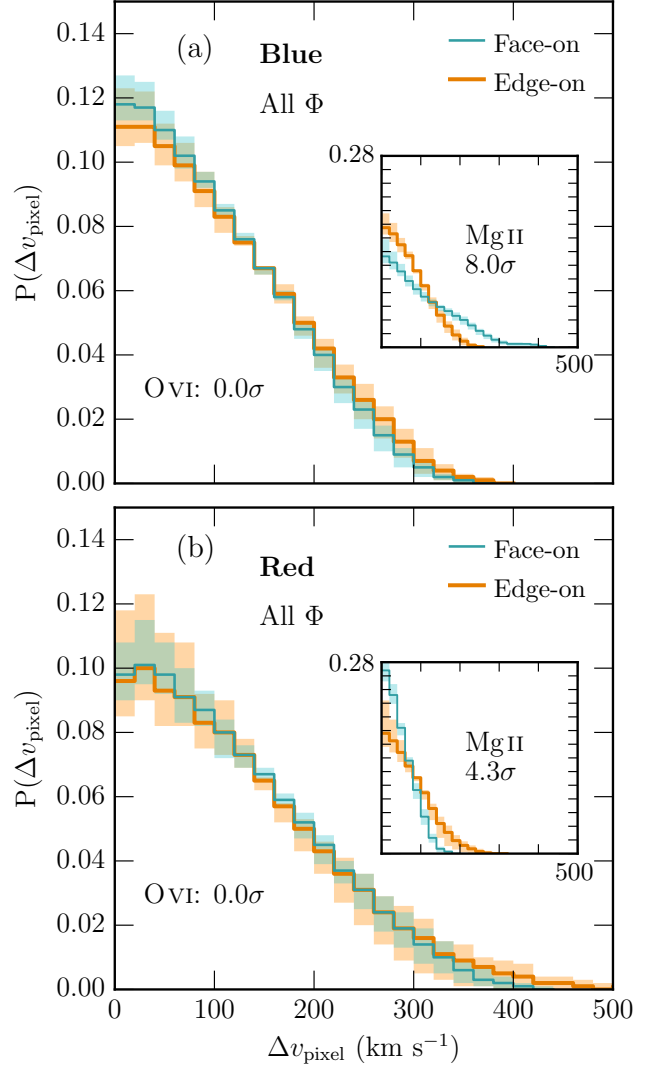


Figure 5. Pixel-velocity TPCFs comparing face-on and edge-on orientations for (a) blue galaxies and (b) red galaxies. The OVI and MgII TPCFs are plotted as shown in Figure 4. The MgII TPCFs are published in MAGIIICAT V, and are rebinned here for comparison. There is no difference in the OVI TPCFs for every subsample comparison, where the largest significance from a chi-squared test is 1.6σ for edge-on galaxies (not plotted). Only the blue, face-on subsample for the MgII TPCFs has a comparable velocity dispersion to OVI, the rest have smaller dispersions.

TPCFs of face-on and edge-on galaxies, where absorbers hosted by edge-on galaxies tend to have larger velocity spreads. However, the significance decreases to 0.9σ when we remove the outlying $W_r(1031) = 0.8 \text{ \AA}$ absorber. This behavior is also opposite what we found with MgII. As stated above, the MgII face-on, minor axis subsample is comparable to OVI.

As we showed in the previous paragraphs, removing the outlying large equivalent width absorber does not change the results in one comparison (Figure 6(b)), but removes the significant difference in another (minor axis, face-on vs edge-on subsamples). This results from the combination that the edge-on, major axis subsample TPCF is slightly more narrow than the rest of the subsamples, but the uncertainties are large enough to overlap with the face-on subsamples, and the uncertainties on the edge-on, minor axis subsample are reduced when the outlier is removed. Given this, we make the assump-

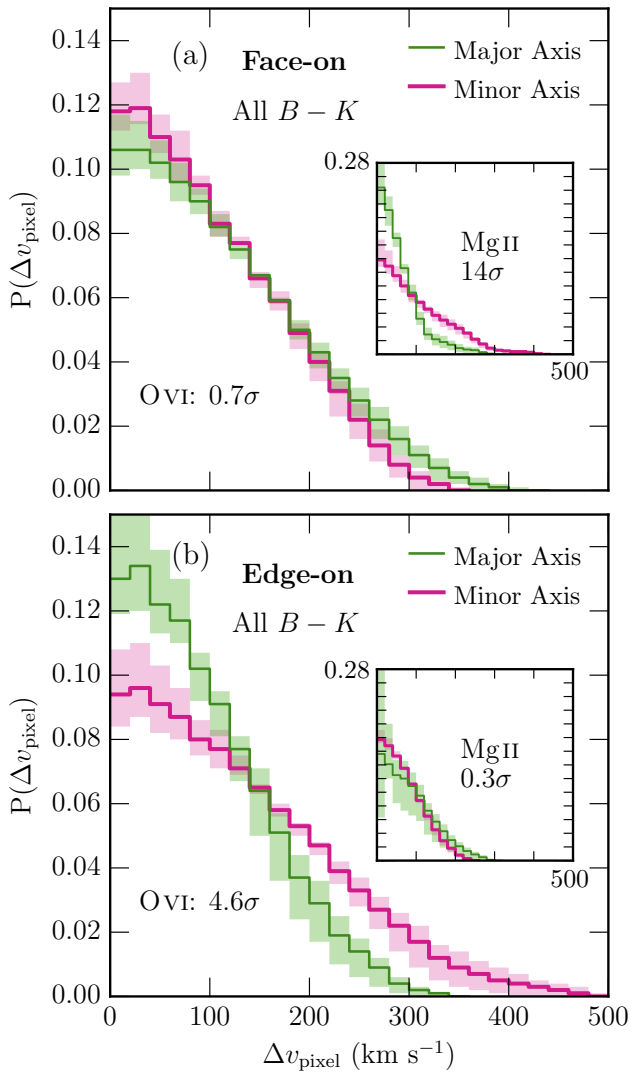


Figure 6. Pixel-velocity TPCFs for (a) face-on galaxies and (b) edge-on galaxies probed along the projected major and minor axes. The TPCFs for the OVI and MgII subsamples are plotted similarly to those in Figure 4. The MgII TPCFs are published in MAGIIICAT V, and are rebinned here for comparison. The OVI TPCFs for face-on galaxies in panel (a) show no difference when the galaxy is probed along the major or minor axis (0.7σ). In panel (b) the OVI TPCF for edge-on galaxies probed along the minor axis have larger velocity dispersions than those along the major axis, corresponding to a 4.6σ significance. This significance drops to 3.4σ when the outlier in OVI equivalent width is removed from the sample, and this remaining significant difference is due to a combination of small uncertainties on the minor axis subsample and the major axis being slightly less extended than the rest of the subsamples.

tion that there are no kinematic differences between these subsamples when the outlying large equivalent width absorber is not included. We also note that a larger sample size would be beneficial in either reducing the uncertainties on the kinematics for the edge-on subsamples along the major and minor axes, or showing more strongly that there is a large variation in the velocity dispersions for these subsamples.

4. DISCUSSION

As we have shown in the previous sections, the kinematics of OVI absorbers are similar regardless of galaxy color, azimuthal angle, and inclination. Compared to our previously published MgII TPCFs (MAGIIICAT IV and V), the

OVI TPCFs are more extended and are much less sensitive to the galaxy properties. In subsamples where we expect outflows to dominate the absorption, MgII and OVI TPCFs are comparable.

The larger velocity spreads for OVI than MgII for nearly all subsamples may be explained if OVI is collisionally ionized. In this case, OVI absorption profiles would be broader than MgII. However, the contrasts between the two ion samples still seem a bit puzzling. If the two ions trace the same gas, then the relative behavior of the TPCFs between the ions should be similar as they are the result of the same baryon cycle processes, i.e., in Figure 5(a), the face-on subsample should be more extended than the edge-on subsample for both OVI and MgII, but this is not the case. If we assume that this scenario is true (we show later that it likely is not), we can examine the several differences between the two samples that may be contributing to our TPCF results.

The OVI sample probes the CGM at larger impact parameters on average ($\langle D \rangle = 86$ kpc) than the MgII sample ($\langle D \rangle = 40$ kpc; see Figure 2; MAGIIICAT IV and V). Simulations by Oppenheimer et al. (2016) show an age–radius anti-correlation with OVI absorption, where the time since the gas was ejected from the galaxy via outflows increases with increasing radii. The lack of a kinematic dependence on orientation in the OVI sample TPCFs may then be a result of the absorbers being located further away from the galaxy, and thus less dependent on the current star formation activity than for the MgII sample. This is strengthened by the finding that the OVI TPCFs show similar behaviors for both blue and red galaxies.

The galaxies hosting OVI absorbers tend to be redder than MgII host galaxies, with $\langle B-K \rangle = 1.66$ and $\langle B-K \rangle = 1.4$, respectively. For MgII, the kinematics of absorbers around redder galaxies are less sensitive to the orientation at which they are located than they are for blue galaxies (for example, see the inset TPCFs in Figures 4 and 5; also see MAGIIICAT V). Additionally, redder galaxies tend to have lower star formation rates and, consequently, are not expected to have active outflows or accretion. Given this, we would expect less of an orientation dependence for the OVI absorbers because they are redder galaxies on average than the MgII sample, which does show an orientation dependence.

The redshift distributions of the two samples are also different. While the galaxies for the MgII sample were located at a median redshift of $\langle z_{\text{gal}} \rangle = 0.656$ ($0.3 < z_{\text{gal}} < 1.0$), the OVI sample has a median of $\langle z_{\text{gal}} \rangle = 0.244$ ($0.1 < z_{\text{gal}} < 0.66$). In this case, the lower redshift galaxies have lower star formation rates (they tend to be redder), and thus have a less active baryon cycle than at higher redshifts. This would result in a weaker dependence of the absorber kinematics on galaxy orientation for the lower redshift OVI sample. Kacprzak et al. (2011a) reported the fraction of systems where MgII absorption velocities were in alignment with the galaxy rotation direction. They found that this fraction decreases by a factor of two from $z \sim 0.5$ to $z \sim 0.1$. Furthermore, they report a factor of three increase at $z \sim 0.1$ compared to $z \sim 0.5$ for MgII absorption spanning both sides of the galaxy systemic velocity. It is possible that CGM kinematics may evolve with redshift; however, we have yet to explore the MgII TPCFs in the lower redshift range probed by the OVI sample because of the lack of high-resolution spectra.

While the differences between the two samples listed above probably do have some effect on our results, we do not think they dominate. The discussion above mostly assumes that

OVI and Mg II trace the same components of the CGM. However, it is more likely that, with their differing ionization states and kinematics, the two ions trace different components of the CGM. This is supported by both observations (e.g., [Werk et al. 2013](#); [Muzahid et al. 2015](#)) and simulations (e.g., [Ford et al. 2014](#); [Churchill et al. 2015](#)). Even for the overlapping seven galaxies in the Mg II and OVI samples with absorption in both ions, the two ions are offset in z_{abs} (defined as the optical depth-weighted median of the absorption) by as little as $\sim 10 \text{ km s}^{-1}$ or as great as $\sim 100 \text{ km s}^{-1}$. These seven absorbers show that the distribution of the gas is different in velocity space between ions.

Using roughly the same sample we use here, [Kacprzak15](#) showed that OVI absorption is preferentially distributed along the major and minor axes of the host galaxies, with non-detected OVI sightlines primarily located between the major and minor axes. The authors suggested that OVI is not mixed throughout the CGM and is confined into outflows along the minor axis and inflows or recycled gas along the major axis. They also showed that the OVI equivalent widths were stronger along the projected minor axis than along the major axis, suggesting that either the column densities, the velocity spreads, or both are larger for absorbers located along the minor axis. These results seem contrary to what we find here with the kinematics.

Since the kinematics of the OVI absorbers are roughly consistent for all galaxy color and orientation combinations, this suggests that OVI may not trace different baryon cycle processes. In simulations, [Ford et al. \(2014\)](#) found that OVI traces gas that was ejected from the galaxy by ancient outflows many Gyr prior to the current epoch, some of which is likely reaccreting onto the galaxy at the time of the mock observations. If this is the case, then the absorbing gas may have plenty of time to mix and form a roughly kinematically uniform OVI halo at all locations about the galaxy. The sizes of OVI absorbers are also predicted to be large, on the order of tens to hundreds of kiloparsecs from photoionization modeling ([Lopez et al. 2007](#); [Muzahid 2014](#); [Hussain et al. 2015](#)), so any kinematic differences with galaxy orientation may be wiped out by the large cloud sizes. This is in contrast to the small, $\sim 10 \text{ pc}$ cloud sizes expected for Mg II (e.g., [Rigby et al. 2002](#); [Crighton et al. 2015](#)). A kinematically uniform OVI halo is therefore reasonable.

The combination of consistent absorber kinematics with orientation and color, the low fraction of absorbing gas in intermediate azimuthal angles from [Kacprzak15](#), and absorption concentrated near the major and minor axes may be the result of differing ionization conditions throughout the CGM. OVI absorbing gas that is located in the intermediate azimuthal angles may be more susceptible to being ionized out of the OVI phase due to lower densities, resulting in lower equivalent widths (or upper limits on the equivalent width) and lower covering fractions. Conversely, higher gas densities due to outflows and inflows along the minor and major axes, respectively, may shield the oxygen from being ionized out of the OVI ionization state and provide more suitable conditions for OVI. If so, higher ionization phases of oxygen may show an orientation dependence in covering fraction and equivalent width, with possibly a higher incidence of gas in the intermediate azimuthal angles when compared to OVI.

5. SUMMARY AND CONCLUSIONS

Using an absorption-selected sample of 29 galaxies ($0.13 < z_{\text{gal}} < 0.66$) from [Kacprzak15](#), we examined the velocity dis-

tribution of OVI absorption as a function of galaxy color, inclination, and azimuthal angle. Each absorber–galaxy pair was identified as part of the “Multiphase Galaxy Halos” survey (e.g., [Kacprzak15](#), [Muzahid et al. 2015, 2016](#)) or obtained from the literature. The galaxies were found within $D \sim 200 \text{ kpc}$ of a background quasar sightline and have redshifts consistent with detected OVI absorption in *HST*/COS quasar spectra. Each galaxy is isolated, with no nearby neighbors within 100 kpc and a line-of-sight velocity separation of 500 km s^{-1} . Galaxies were modeled using GIM2D to obtain their inclinations, morphologies, and the azimuthal angle at which the background quasar probes the CGM relative to the projected galaxy major axis. We use the pixel-velocity TPCF method described in [MAGIICAT IV and V](#) for Mg II on our OVI absorbers, and compare the results between both Mg II from our previous work and the OVI here. Our findings include the following:

1. In general, the OVI TPCFs are more extended than for Mg II, which is expected if the OVI is collisionally ionized. In orientations in which outflows are expected, such as blue, face-on galaxies probed along the minor axis, the TPCFs are comparable between ions and show similar velocity dispersions.
2. Given the vastly different kinematics of the OVI absorbers compared to Mg II, it is very likely that the two ions trace different components of the CGM. In fact, the seven galaxies that have both detected OVI and Mg II show values of z_{abs} (optical depth-weighted median of absorption) that can be offset by up to 100 km s^{-1} .
3. The OVI absorbers have similar velocity dispersions (Chi-squared test result of $< 1\sigma$) regardless of galaxy color, inclination angle, and azimuthal angle, indicating that the gas is not strongly influenced by the present star formation activity in the galaxy (i.e., possibly deposited into the CGM by “ancient outflows”). This is despite the findings of [Kacprzak15](#) that OVI is preferentially observed along the projected major and minor axes of galaxies, which are frequently associated with accretion and outflows, respectively.
4. The TPCF of the minor axis, edge-on subsample (likely dominated by outflowing material) may be more extended than the major axis, edge-on subsample (4.6σ). This large velocity separation tail is mostly due to a single large equivalent width absorber with a large velocity spread, which is classified as a large-scale galactic outflow by [Muzahid et al. \(2015\)](#). Removing the outlier still results in a significant difference (3.4σ), however this significance is driven more by the major axis, edge-on subsample TPCF being slightly more narrow. Thus, the significant differences found in [Figure 6](#) are likely not real.
5. The uniform OVI kinematics with galaxy color and orientation, and the azimuthal location preference of the OVI absorbers point to ionization effects in the CGM. The gas giving rise to OVI may be uniformly distributed throughout the CGM, but lower densities in intermediate azimuthal angles ($30^\circ < \Phi < 60^\circ$) where outflows and accretion are less likely to occur may result in the oxygen being ionized out of the OVI phase.

To better understand how the kinematics of Mg II and OVI compare, it would be useful to form a large sample of galaxies with both OVI and Mg II absorption detected in high resolution quasar spectra. As our samples stand now, it is not

straightforward to compare the two ion samples to each other due to differing galaxy property distributions for the separate absorbing samples. Measuring the multiphase kinematics for a set of galaxies like this is necessary for understanding the multiphase CGM.

Lastly, observing the CGM in higher ionization states as a function of galaxy properties is important if the azimuthal angle distribution of O VI is mainly due to differing ionization conditions. The higher ionization states may also show an azimuthal preference, where the incidence rate of higher ionization absorbers may be larger in the intermediate azimuthal angles than O VI. While it is not currently feasible to study ions such as O VII and O VIII because they are located in the x-ray regime, Ne VIII is observable in the UV. This kinematics–galaxy orientation study could be done with Ne VIII once a large enough sample is obtained.

Support for this research was provided by NASA through grants HST GO-13398 from the Space Telescope Science Institute, which is operated by the Association of Universities for Research in Astronomy, Inc., under NASA contract NAS5-26555. G.G.K. acknowledges the support of the Australian Research Council through the award of a Future Fellowship (FT140100933). M.T.M. thanks the Australian Research Council for Discovery Project grant DP130100568 which supported this work.

REFERENCES

- Bordoloi, R., Lilly, S. J., Kacprzak, G. G., & Churchill, C. W. 2014a, *ApJ*, 784, 108
- Bordoloi, R., Lilly, S. J., Knobel, C., et al. 2011, *ApJ*, 743, 10
- Bordoloi, R., Lilly, S. J., Hardmeier, E., et al. 2014b, *ApJ*, 794, 130
- Bouché, N., Hohensee, W., Vargas, R., et al. 2012, *MNRAS*, 426, 801
- Bouché, N., Murphy, M. T., Kacprzak, G. G., et al. 2013, *Science*, 341, 50
- Churchill, C. W., Trujillo-Gomez, S., Nielsen, N. M., & Kacprzak, G. G. 2013, *ApJ*, 779, 87
- Churchill, C. W., Vander Vliet, J. R., Trujillo-Gomez, S., Kacprzak, G. G., & Klypin, A. 2015, *ApJ*, 802, 10
- Churchill, C. W., & Vogt, S. S. 2001, *AJ*, 122, 679
- Crighton, N. H. M., Hennawi, J. F., Simcoe, R. A., et al. 2015, *MNRAS*, 446, 18
- Ford, A. B., Davé, R., Oppenheimer, B. D., et al. 2014, *MNRAS*, 444, 1260
- Hussain, T., Muzahid, S., Narayanan, A., et al. 2015, *MNRAS*, 446, 2444
- Johnson, S. D., Chen, H.-W., & Mulchaey, J. S. 2013, *MNRAS*, 434, 1765
- . 2015, *MNRAS*, 449, 3263
- Kacprzak, G. G., Churchill, C. W., Barton, E. J., & Cooke, J. 2011a, *ApJ*, 733, 105
- Kacprzak, G. G., Churchill, C. W., Ceverino, D., et al. 2010, *ApJ*, 711, 533
- Kacprzak, G. G., Churchill, C. W., Evans, J. L., Murphy, M. T., & Steidel, C. C. 2011b, *MNRAS*, 416, 3118
- Kacprzak, G. G., Churchill, C. W., & Nielsen, N. M. 2012, *ApJ*, 760, L7
- Kacprzak, G. G., Muzahid, S., Churchill, C. W., Nielsen, N. M., & Charlton, J. C. 2015, *ApJ*, 815, 22
- Kacprzak, G. G., Martin, C. L., Bouché, N., et al. 2014, *ApJ*, 792, L12
- Lan, T.-W., Ménard, B., & Zhu, G. 2014, *ApJ*, 795, 31
- Lilly, S. J., Carollo, C. M., Pipino, A., Renzini, A., & Peng, Y. 2013, *ApJ*, 772, 119
- Lopez, S., Ellison, S., D’Odorico, S., & Kim, T.-S. 2007, *A&A*, 469, 61
- Martin, C. L., Shapley, A. E., Coil, A. L., et al. 2012, *ApJ*, 760, 127
- Mathes, N. L., Churchill, C. W., Kacprzak, G. G., et al. 2014, *ApJ*, 792, 128
- Muzahid, S. 2014, *ApJ*, 784, 5
- Muzahid, S., Kacprzak, G. G., Charlton, J. C., & Churchill, C. W. 2016, *ApJ*, 823, 66
- Muzahid, S., Kacprzak, G. G., Churchill, C. W., et al. 2015, *ApJ*, 811, 132
- Nielsen, N. M., Churchill, C. W., & Kacprzak, G. G. 2013a, *ApJ*, 776, 115
- Nielsen, N. M., Churchill, C. W., Kacprzak, G. G., & Murphy, M. T. 2013b, *ApJ*, 776, 114
- Nielsen, N. M., Churchill, C. W., Kacprzak, G. G., Murphy, M. T., & Evans, J. L. 2015, *ApJ*, 812, 83
- . 2016, *ApJ*, 818, 171
- Oppenheimer, B. D., & Davé, R. 2008, *MNRAS*, 387, 577
- Oppenheimer, B. D., Crain, R. A., Schaye, J., et al. 2016, *ArXiv e-prints*
- Peeples, M. S., Werk, J. K., Tumlinson, J., et al. 2014, *ApJ*, 786, 54
- Prochaska, J. X., Weiner, B., Chen, H.-W., Mulchaey, J., & Cooke, K. 2011, *ApJ*, 740, 91
- Rigby, J. R., Charlton, J. C., & Churchill, C. W. 2002, *ApJ*, 565, 743
- Rubin, K. H. R., Prochaska, J. X., Koo, D. C., & Phillips, A. C. 2012, *ApJ*, 747, L26
- Rubin, K. H. R., Prochaska, J. X., Koo, D. C., et al. 2014, *ApJ*, 794, 156
- Rubin, K. H. R., Weiner, B. J., Koo, D. C., et al. 2010, *ApJ*, 719, 1503
- Savage, B. D., Kim, T.-S., Wakker, B. P., et al. 2014, *ApJS*, 212, 8
- Simard, L., Willmer, C. N. A., Vogt, N. P., et al. 2002, *ApJS*, 142, 1
- Steidel, C. C., Kollmeier, J. A., Shapley, A. E., et al. 2002, *ApJ*, 570, 526
- Stewart, K. R., Kaufmann, T., Bullock, J. S., et al. 2011, *ApJ*, 738, 39
- Stocke, J. T., Keeney, B. A., Danforth, C. W., et al. 2013, *ApJ*, 763, 148
- Thom, C., Werk, J. K., Tumlinson, J., et al. 2011, *ApJ*, 736, 1
- Tumlinson, J., Thom, C., Werk, J. K., et al. 2011, *Science*, 334, 948
- Wakker, B. P., & Savage, B. D. 2009, *ApJS*, 182, 378
- Werk, J. K., Prochaska, J. X., Thom, C., et al. 2012, *ApJS*, 198, 3
- . 2013, *ApJS*, 204, 17
- Zibetti, S., Ménard, B., Nestor, D. B., et al. 2007, *ApJ*, 658, 161